Downward-Looking Linear Array Three-Dimensional SAR Imaging Based on the Two-Dimensional Mismatch Compensation

Le Kang [ID], Tian-chi Sun, Ying Luo [ID], *Member, IEEE*, Qun Zhang [ID], *Senior Member, IEEE*, and Jia-cheng Ni [ID]

Abstract—For downward-looking linear array (DLLA) three-dimensional (3-D) synthetic aperture radar (SAR), it is necessary to realize the super-resolution in both azimuth and cross-track direction due to the limited lengths of the synthetic aperture and the linear array. As all the scatterers are assumed on the uniform grids, the cross-track super-resolution can be achieved by 1-D compressed sensing. In the real imaging system, however, the gridding error should be considered because the biased scatterers lead to the mismatch of the measurement matrix and affect the imaging performance. The 1-D mismatch in cross-track direction has been solved by atomic norm minimization and off-grid sparse Bayesian inference. With the development of the super-resolution methods, the 2-D super-resolution in both azimuth and cross-track direction is realized by the 2-D compressed sensing (CS) algorithms. To solve the 2-D mismatch problem, a novel 2-D mismatch compensation method for DLLA 3-D SAR is proposed. Instead of converting the 2-D matrix signals to the 1-D vectors, the proposed method directly processes the 2-D mismatch with 2-D joint model. Furthermore, the 2-D joint model with 2-D mismatch is simplified as a normal sparse linear model, which is suitable for most of the CS reconstruction algorithms. It can not only provide better reconstruction performance but also reduce the memory cost and computation load. Finally, the simulation experiments are shown to demonstrate the validity of the proposed method.

Index Terms—Array synthetic aperture radar (SAR), compressed sensing (CS), measurement matrix mismatch, super-resolution, three-dimensional (3-D) synthetic aperture radar (SAR).

I. INTRODUCTION

THREE-DIMENSIONAL synthetic aperture radar (3-D SAR), as a development trend of the conventional SAR,

Le Kang, Tian-chi Sun, and Jia-cheng Ni are with the Institute of Information and Navigation, Air Force Engineering University, Xi'an 710077, China and with the Collaborative Innovation Center of Information Sensing and Understanding, Xi'an 710077, China (e-mail: 18810495946@163.com; triplemeteornj@163.com; littlenjc@sina.com).

Ying Luo and Qun Zhang are with the Institute of Information and Navigation, Air Force Engineering University, Xi'an 710077, China with the Collaborative Innovation Center of Information Sensing and Understanding, Xi'an 710077, China, and also with the Key Laboratory for Information Science of Electromagnetic Waves (Ministry of Education), Fudan University, Shanghai 200433, China (e-mail: luoying2002521@163.com; zhangqunnus@gmail.com).

has attracted wide attention in recent years [1], [2]. Nowadays, the 3-D SAR can mainly be categorized into three different frames, including TomoSAR, CSAR, and array SAR [3]–[5]. As a kind of array SAR, the downward-looking linear array (DLLA) 3-D SAR can synthesize a 2-D plane array and obtain the 3-D resolution of the imaging scene. With linear array antennas distributed along the wing of the rectilinearly moving platform and the downward-looking imaging geometry, ONERA [6] and ARTINO [7], the representative systems of DLLA 3-D SAR, can generate the 3-D scatterers distribution and scattering properties of the directly overflown scene. At first, the imaging algorithms of DL sparse LA (DLSLA) 3-D SAR, e.g., 3-D range migration algorithm [8], 3-D chirp scaling algorithm [9], 3-D back-projection algorithm [10], and 3-D polar format algorithm [11], are proposed by extending the conventional 2-D SAR imaging algorithms. In these algorithms, the 3-D resolution of DLLA 3-D SAR is obtained by applying the pulse compression in the range domain, virtual aperture synthesis with platform movement in azimuth domain, and linear array aperture synthesis in cross-track domain. However, the length limitations of synthetic aperture and linear array lead to the poor resolution in the azimuth direction and the cross-track direction, respectively [12], [13].

Except for improving resolution by wider synthetic aperture and longer linear array, many super-resolution methods are introduced to DLLA 3-D SAR imaging, e.g., spectral estimation [14] and compressed sensing (CS) [15]. To acquire the cross-track super-resolution with the uniform linear array, an imaging algorithm based on the fast Fourier transform and multiple signals classification is proposed, which transforms the cross-track imaging process into the problem of spectral estimation [16]. Moreover, a calibration method based on the time-divided active calibrators is proposed to estimate and correct the virtual element position errors [17]. Besides the super-resolution imaging, it is an important problem to reduce the number of antenna elements on the linear array to simplify the hardware of DLLA 3-D SAR. Since the signal of DLLA 3-D SAR is sparse in the cross-track domain [18], and the sparse signals from limited measurements can be exactly recovered with a high probability by CS [19], CS is widely used in the cross-track domain of DLLA 3-D SAR [20]–[22]. In [20], a new 3-D imaging strategy based on the Bayesian CS is proposed for down-looking MIMO array SAR, which transforms the cross-track imaging process into a problem of sparse signal reconstruction from noisy measurements. To

realize the cross-track super-resolution with a nonuniform linear array, the truncated SVD-based CS method is proposed [21]. In [22], a DLSLA 3-D SAR image reconstruction algorithm that combines polar formatting and *L*1 regularization is presented, which can be employed to airborne DLLA 3-D SAR with nonuniform and sparse cross-track virtual phase centers.

For DLLA 3-D SAR cross-track reconstruction, the measurement matrix is mainly determined by the configuration of the antenna phase centers and the grids discretization strategy of the imaging region, which means that the sparse signal must be represented on the predefined discretized grids [16]–[17], [20]–[22]. However, for a practical scene, the scatterers are scarcely located on the exact grids, which will cause the problem of basis mismatch [23]–[24]. In addition, the gridding error cannot be reduced by discretizing the grids densely since the denser grids may cause the poorer restricted isometry property (RIP) of the measurement matrix, which affects the reconstruction performance in CS methods [25]. Considering the basis mismatch problem, the methods based on atomic norm [26]–[28] transform the cross-track processing into the semidefinite programming problem. In another kind of approach, the basis mismatch of cross-track processing is regarded as the parametric sparse representation, which is solved by off-grid sparse Bayesian inference (OGSBI) [29], [30].

However, these imaging algorithms based on the CS theory are only used for 1-D processing to improve the cross-track resolution. Due to the limited lengths of the synthetic aperture and the linear array, it is necessary to realize the super-resolution in both azimuth and cross-track direction. The 2-D super-resolution approaches in DLLA 3-D SAR can be mainly divided into two ways, e.g., the vectorization model and the joint model. In the vectorization model, although the 3-D signal after range compression is divided into a series of equal-range 2-D slices, the 2-D slices are still needed to be converted into 1-D vectors for CS reconstruction. Utilizing the vectorization model in azimuth and cross-track plane, the 2-D super-resolution imaging of "one-active" LASAR is built in a CS framework and solved by convex optimization [31]. Combining the vectorization model with DLLA 3-D SAR, several studies deal with each slice separately using the different CS algorithms [32], [33]. However, the computational cost and memory consumption of the vectorization model are terrible in these articles [31]–[33]. In the joint model, each 2-D slice of azimuth and the cross-track plane should be regarded as an entirety, which can solve the problem brought by the vectorization operation. Applying the 2-D joint CS in DLLA 3-D SAR, the 3-D imagery with super-resolutions in the azimuth and cross-track directions can be acquired by the efficient 2-D smoothed l_0 norm (SL0) algorithm [12]. Moreover, matrix completion for DLLA 3-D SAR is proposed for the undersampled azimuth-cross-track data [13]. For the above 2-D super-resolution imaging approaches, the imaging scene is discretized with the grids. Since the scatterers are continuously distributed in the azimuth-cross-track plane, the gridding errors between the real scatterers and grid points are always existing. Therefore, the mismatch problem should be extended to 2-D.

In this article, a novel 2-D mismatch compensation method for DLLA 3-D SAR is proposed. Instead of converting the 2-D
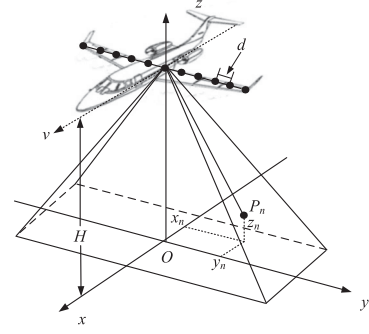

Fig. 1. DLLA 3-D SAR imaging mode.

matrix signals to the 1-D vectors, the proposed method directly builds the 2-D mismatch compensation model based on the 2-D joint model. It can not only provide better reconstruction performance but also reduce the memory cost and computation load. Furthermore, the linear model with 2-D mismatch is simplified as a normal sparse linear model, which is suitable for most of the CS reconstruction algorithms. Here, we chose the 2-D SL0 algorithm to solve the imaging model. Finally, the validity of the proposed method is demonstrated by the simulation experiments in which the simulation data are generated by the real scene and the corresponding digital elevation model (DEM).

This article is organized as follows. Section II formulates the signal model of DLLA 3-D SAR, and Section III reviews the mismatch problem in cross-track direction briefly. In Section IV, the DLLA 3-D SAR imaging algorithm based on the 2-D mismatch compensation model is presented. The simulation experiments are carried out in Section V to evaluate the proposed algorithm. Finally, Section VI concludes this article.

II. SIGNAL MODEL

The imaging geometry of DLLA 3-D SAR is shown in Fig. 1, The platform is supposed to fly at the altitude H along the flight line (*X*-axis) with the velocity v. The linear array is mounted underneath the wings along the cross-track direction (*Y*-axis), and it is constituted by N antenna elements equally spaced with the distance d. The height direction (i.e., the range direction) is denoted by the *Z*-axis. The center of the 3-D imaging scene is set as the origin of the coordinate O. At slow time t_m, the coordinate of the *n*th antenna element is (x_m, y_n, H), where $x_m = vt_m$, $y_n = -(N-1)d/2 + (n-1)d$. According to the geometry, the instantaneous distance from the *n*th antenna element to the point scatterer $P_k(x_k, y_k, z_k)$ can be expressed as

$$R(t_m, y_n) = \sqrt{(vt_m - x_k)^2 + (y_n - y_k)^2 + (H - z_k)^2}. \tag{1}$$

As the point scatterer P_k is located at the far field of the antenna, the instantaneous distance R can be rewritten as

$$R(t_m, y_n) \approx R_0 + \frac{x_m^2 - 2vt_m x_k}{2R_0} + \frac{y_n^2 - 2y_n y_k}{2R_0} \tag{2}$$

where $R_0 = (x_k^2 + y_k^2 + (H - z_k)^2)^{1/2}$ is the projection of the instantaneous range on the zero Doppler plane.

In the monostatic mode, the transmitting and receiving antenna elements are active simultaneously. The antenna element transmits a linear frequency modulation signal with the center frequency f_c in turn and receives the incoming echo signal from the reflection by the scatterers. The echo signal received from the nth antenna can be written as

$$s(t, t_m, y_n) = \mathrm{rect}\left(\frac{t - 2R/c}{T_r}\right) \mathrm{rect}\left(\frac{t_m - 2x_k/v}{T_a}\right)$$
$$\times \gamma_k \cdot \exp\left(j\pi K_r\left(t - \frac{2R}{c}\right)^2 - j\frac{4\pi}{\lambda}R\right)$$
$$(3)$$

where t is the fast time, $\mathrm{rect}(\cdot)$ is the unit rectangular function, T_r is the pulsewidth, T_a is the observing duration, γ_k is the scattering coefficient of the point scatterer, $\lambda = c/f_c$ is the wavelength and c is the speed of light, and K_r is the chirp rate.

The processing of (3) can be divided into three steps, including range compression, azimuth compression, and cross-track compression. The range compression of (3) can be expressed as

$$s_r(t, t_m, y_n) = \mathrm{IFT_r}\left[\mathrm{FT_r}\left[S(t, t_m, y_n)\right] \cdot H_r \cdot H_{rma} \cdot H_{rmc}\right]$$
$$= \mathrm{sinc}\left(T_r K_r\left(t - \frac{2R_0}{c}\right)\right) \mathrm{rect}\left(\frac{t_m - 2x_k/v}{T_a}\right)$$
$$\cdot \gamma_k \exp\left(-j\frac{4\pi}{\lambda}R\right)$$
$$(4)$$

where FT_r and IFT_r denote the Fourier transformation and inverse Fourier transformation of range direction, $H_r(f_r) = \mathrm{rect}(f_r/T_r K_r)\exp(j\pi f_r^2/K_r)$ is the range matched filter function, H_{rma} and H_{rmc} denote the range migration correction function in the azimuth and cross-track direction, respectively [20].

The azimuth compression of (4) can be expressed as

$$s_a(t, t_m, y_n) = \mathrm{IFT_a}\left[\mathrm{FT_a}\left[S_r(t, t_m, y_n)\right] \cdot H_a\right]$$
$$= \mathrm{sinc}(T_r K_r(t - 2R_0/c))\mathrm{sinc}(T_a K_a(t_m - 2x_k/c))$$
$$\cdot \gamma_k \exp\left(-j\frac{2\pi(y_n^2 - 2y_n y_k)}{\lambda R_0}\right) \exp\left(-j\frac{4\pi}{\lambda}R_0\right)$$
$$(5)$$

where $K_a = 2v^2/\lambda R_0$, FT_a and IFT_a denote the Fourier transformation and inverse Fourier transformation of azimuth direction, and $H_a(f_a) = \mathrm{rect}(f_a/T_a K_a)\exp(j\pi f_a^2/K_a)$ is the azimuth matched filter function.

After the 2-D imaging process in the range and azimuth directions, the quadratic phase term and the constant phase term in (5) can be compensated as y_n and R_0 are known. Then, the signal in the range–azimuth cell can be expressed as

$$s_c(t, t_m, y_n) = \sum_{k=1}^{K} \gamma_k(t, t_m) \exp\left(j2\pi f_k y_n\right)$$
$$(6)$$

where $\gamma_k(t, t_m)$ denote the scattering coefficient of the scatterer P_k, and $f_k = 2y_k/\lambda R_0$.

III. REVIEW OF MISMATCH PROBLEM IN CROSS-TRACK DIRECTION

At first, several previous research articles on the DLLA 3-D SAR imaging focus on cross-track super-resolution based on CS. After the range and azimuth compression, the widely used signal model of each range and azimuth cell is [10], [16], [20]–[22], [26]–[28], [30]

$$s_c(y_n) = \sum_{k=1}^{K} \gamma_k \exp\left\{j4\pi\frac{y_n y_k}{\lambda R_0}\right\}.$$
$$(7)$$

As the number of intersections of a line and a target is limited, the scattering centers in a range and azimuth cell are generally sparse distributed. Therefore, the cross-track imaging of (7) can be regarded as the problem of sparse signal reconstruction.

Suppose that the cross-track direction is discretized as equal grids $y = [y_1, y_2, \ldots, y_Q]$, and the real locations of scattering centers in the cross-track direction are $\hat{y} = [\hat{y}_1, \hat{y}_2, \ldots, \hat{y}_K]$. As all the scattering centers are assumed on uniform grids without any gridding error, i.e., $\hat{y} \subset y$, (7) can be rewritten as

$$s_c = R\gamma + n$$
$$(8)$$

where $s_c = [s_c(y_1), s_c(y_2), \ldots, s_c(y_N)]^T$ is the signal vector, $R = [r_1, r_2, \ldots, r_Q]$, $r_q = [j4\pi y_1 y_q/\lambda R_0, \ldots, j4\pi y_N y_q/\lambda R_0]^T$, and $\gamma = [\gamma_1, \ldots, \gamma_Q]^T$ and n are the scattering coefficients vector and the noise vector, respectively. To provide high resolution in the cross-track direction, $Q \gg N$ should be satisfied. So, (8) is an underdetermined linear problem, which can be solved by the following model:

$$\min L(\gamma)\ \mathrm{s.t.}\ \|s - R\gamma\|_2^2 \leq \eta_0$$
$$(9)$$

where $L(\gamma)$ is the penalty function with the sparsity of scattering centers and η_0 is a small threshold. Since the sparse vector is a random variable in the noise environment, the form of penalty function is related to the prior probability distribution of the sparse vector. For example, the prior probability distribution of scattering centers obeys the Laplace of order $p\ (0 \leq p \leq 1)$ in the conventional SAR or ISAR imaging, and the penalty function can be expressed as $\|X\|_p^p$.

In the real imaging system, however, $\hat{y} \not\subset y$ since the scattering centers are continuously distributed along the cross-track direction. The gridding error should be considered because the biased scattering centers lead to the mismatch of the measurement matrix R and affect the performance of imaging schemes. In addition, the gridding error cannot be reduced by discretizing the grids densely since the denser grids may cause a poorer RIP of the measurement matrix R, which affects the reconstruction performance in the CS methods. For the above mismatch problem in the cross-track direction, the solving approaches can be mainly divided into two ways in the signal processing field.

1) Atomic norm minimization [26]–[28], which is referred to as continuous CS, has been proposed to work in the continuous domain to eliminate the mismatch problem in cross-track reconstruction. However, due to the atomic norm minimization is solved by semidefinite programming, the computation cost of the gridless CS method is too expensive for imaging or video processing. Moreover, the resolution of the gridless CS method
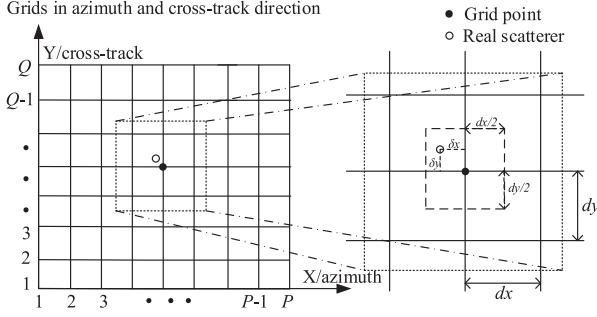
Fig. 2. Discretized imaging scene in any range cell.

based on the atomic norm is generally a few times the Rayleigh resolution and not suitable for practical applications.

2) Based on the approximation of series expansion, the other kind of approaches, in which the basis mismatch problem is transformed into parametric sparse representation [29], are more efficient. While the remainder term of the expansion can be ignored without losing accuracy when it is lower than the noise error, this kind of method has been preliminarily introduced in DLLA 3-D SAR cross-track reconstruction [30].

After padding zero, the real position of the scatterers in the cross-track direction can be denoted by $\hat{y} = [\hat{y}_1, \hat{y}_2, \ldots, \hat{y}_Q]$. The off-grid distance in the cross-track direction is $\delta y_q = \hat{y}_q - y_q$, where y_q is the nearest grid point of the scattering center in the cross-track direction and $\delta y_q \in [-\frac{1}{2}d_y, \frac{1}{2}d_y]$. For the real position $\hat{y}_q$, the column of the measurement matrix can be approximated by the Taylor expansion

$$r_q(\hat{y}_q) \approx r_q(y_q) + r'_q \delta y_q \tag{10}$$

where r'_q is the first-order derivative of $r_q(y_q)$. Define $R' = [r'_1, r'_2, \ldots, r'_Q]$ and $\Lambda = \mathrm{diag}([\delta y_1, \ldots, \delta y_Q])$, and the modified expression of (8) is given by

$$s_c = R(\Lambda)\gamma + n \tag{11}$$

where $R(\Lambda) = R + R'\Lambda$ is the modified measurement matrix.

The model in (11) can be solved by OGSBI [29].

IV. Two-Dimensional Mismatch Compensation Model

A. Two-Dimensional Mismatch Problem

The CS-based super-resolution imaging can be used in both the cross-track domain and the azimuth domain. Therefore, the mismatch problem is extended to the 2-D form.

Recalling the signal after range compression, it can be further expressed as

$$s_r(t, t_m, y_n) = \sum_{k=1}^{K} \gamma_k(t) \exp\left(-j2\pi \frac{x_m^2 + y_n^2}{\lambda R_0}\right)$$

$$\times \exp\left\{j4\pi \frac{x_m x_k}{\lambda R_0}\right\} \exp\left\{j4\pi \frac{y_n y_k}{\lambda R_0}\right\}. \tag{12}$$

As shown in Fig. 2, the imaging scene can be discretized with the grid width d_x in the azimuth direction and d_y in the cross-track direction, and the grid point is located at $(x_p = pd_x, y_q = qd_y)$, where $p = 1, 2, \ldots, P$ and $q = 1, 2, \ldots, Q$. Then, the locations of the grids are $x = [x_1, x_2, \ldots, x_P]$ in the azimuth direction and $y = [y_1, y_2, \ldots, y_Q]$ in the cross-track direction. The matrix of the scattering coefficient is $\Omega \in \mathbb{C}^{P \times Q}$.

The independent quadratic phase terms in (12) can be removed by deramping operation, and the deramping function is given by $H_{\mathrm{der}} = \exp\left(-j2\pi(x_m^2 + y_n^2)/\lambda R_0\right)$. Assuming that all the scattering centers are on uniform grids without any gridding error, (12) can be rewritten as the following discrete form:

$$S = \sum_{p=1}^{P} \sum_{q=1}^{Q} \gamma_{p,q} \exp\left\{j4\pi \frac{x_m x_p}{\lambda R_0}\right\} \exp\left\{j4\pi \frac{y_n y_q}{\lambda R_0}\right\} \tag{13}$$

where $\gamma_{p,q} = \gamma_k$ if the scatterer P_k is on the grid point (p, q); otherwise, $\gamma_{p,q} = 0$. In the majority of cases, the density of the grid should be sufficient to provide the 2-D high resolution, which means $P \gg M$ and $Q \gg N$. The matrix form of the signal in (13) is $S \in \mathbb{C}^{M \times N}$.

Since the scatterers are continuously distributed in the azimuth-cross-track plane, the gridding errors between the real scatterers and grid points are always existing, as shown in Fig. 2. There is only one scatterer in the range of $\pm \frac{1}{2} d_x$ and $\pm \frac{1}{2} d_y$ around any grid point due to the limitation of resolution. For a scattering center located at $(\hat{x}_p, \hat{y}_q)$, the gridding error between the real scattering center and the nearest grid point (x_p, y_q) is $(\delta x_p = \hat{x}_p - x_p, \delta y_q = \hat{y}_q - y_q)$. Considering the 2-D mismatch problem, the corrected signal should be written as

$$\hat{S} = \sum_{p=1}^{P} \sum_{q=1}^{Q} \gamma_{p,q} \exp\left\{j4\pi \frac{x_m \hat{x}_p}{\lambda R_0}\right\} \exp\left\{j4\pi \frac{y_n \hat{y}_q}{\lambda R_0}\right\}. \tag{14}$$

As shown in (13) and (14), the antenna position y_n and the grid position y_q hold as a Fourier transform pair. Then, the measurement matrix is a partial Fourier matrix, which is affected both by the position of antennas and the grid. As a result, the sparse recovery performance varies with the change of the relative position between the antennas and the grids. Generally, the antenna positions are determined before imaging, and the grid positions should be initialized in the sparse imaging algorithm. If the grid interval is too large, the sparse recovery performance will degrade since the gridding error will be more serious. When the grid interval is smaller, the sparse recovery performance will improve because the gridding error is smaller than the grid interval. However, the sparse recovery performance cannot be improved by reducing the grid interval endlessly because the denser grids may cause the poorer RIP of the measurement matrix, which also affects the sparse recovery performance [25].

Equation (14) is one of the series of equal-range 2-D slices. Due to the limited lengths of the synthetic aperture and the linear array, it is necessary to realize the super-resolution in each 2-D slice. The 2-D super-resolution approaches in DLLA 3-D SAR can be mainly divided into two ways. One way is to convert the 2-D slices to 1-D vectors for CS reconstruction, which is

based on the vectorization model. The other way is to directly reconstruct the slices by 2-D CS, which is based on the joint model. In different kinds of super-resolution models, the 2-D mismatch compensation models are different.

B. Vectorization Model of the 2-D Mismatch Compensation

For any matrix $A = [a_{mn}] \in \mathbb{C}^{M \times N}$, the vectorization operation is generally defined as

$$\text{vec}(A) = [a_1, \ldots, a_i, \ldots, a_I]^T, \quad i = (m-1) \cdot N + n. \tag{15}$$

After transforming the target area and the echo data to column vectors as $\boldsymbol{\gamma} = \text{vec}(\boldsymbol{\Omega}) \in \mathbb{C}^{PQ \times 1}$ and $s = \text{vec}(S) \in \mathbb{C}^{MN \times 1}$, (13) can be rewritten as

$$s = \boldsymbol{H}\boldsymbol{\gamma} + n \tag{16}$$

where $\boldsymbol{H} = (h_1, h_2, \ldots, h_{MN})^T$, $h_i = (h_{i,1}, h_{i,2}, \ldots, h_{i,PQ})$, and $h_{nm,pq} = \exp\left(j4\pi\left(\frac{md_x}{\lambda R_0}x_p + \frac{nd_y}{\lambda R_0}y_q\right)\right)$. $\boldsymbol{H}$ is the basis matrix to map the echo data to the super-resolution image. If the locations of the grid points $x = [x_1, x_2, \ldots, x_{PQ}]$ and $y = [y_1, y_2, \ldots, y_{PQ}]$ are regarded as the parameters of the basis matrix $\boldsymbol{H}$, the parametric sparse representation model of (16) can be rewritten as

$$s = \boldsymbol{H}(x, y)\boldsymbol{\gamma} + n. \tag{17}$$

Equation (17) can be solved by any CS algorithm directly, as x and y are known.

However, as locations of the real scatterers are denoted by $\hat{x} = [\hat{x}_1, \hat{x}_2, \ldots, \hat{x}_{PQ}]$ and $\hat{y} = [\hat{y}_1, \hat{y}_2, \ldots, \hat{y}_{PQ}]$, the corrected signal can be expressed as

$$\hat{s} = \boldsymbol{H}(\hat{x}, \hat{y})\boldsymbol{\gamma} + n. \tag{18}$$

Equation (18) cannot be solved directly since $\hat{x}$ and $\hat{y}$ are unknown. To separate the assumed location (x, y) and the gridding error $(\delta x, \delta y)$, the 2-D Taylor expression of $\boldsymbol{H}(\hat{x}, \hat{y})$ can be written as

$$\boldsymbol{H}(\hat{x}, \hat{y}) = \boldsymbol{H}(x, y) + \left((\hat{x} - x)\frac{\boldsymbol{H}(x, y)}{\partial \hat{x}} + (\hat{y} - y)\frac{\boldsymbol{H}(x, y)}{\partial \hat{y}}\right)$$
$$+ O\left(\left|(\hat{x} - x)\frac{\boldsymbol{H}(x, y)}{\partial \hat{x}} + (\hat{y} - y)\frac{\boldsymbol{H}(x, y)}{\partial \hat{y}}\right|^2\right). \tag{19}$$

According to (14), the model of (18) can be specifically expressed as (20) shown at bottom of next page. The second term of (20) can be rewritten as

$$\sum_{p=1}^{P}\sum_{q=1}^{Q}\gamma_{pq}\exp\left(j4\pi\left(\frac{x_m}{\lambda R_0}x_p + \frac{y_n}{\lambda R_0}y_q\right)\right)$$
$$\times \left(j4\pi\frac{x_m\delta x_{pq}}{\lambda R_0}\right) = \boldsymbol{H}_1(x, y)\boldsymbol{\gamma}_1$$

$$\boldsymbol{H}_1(x, y) = (h_1^1, h_2^1, \ldots, h_{MN}^1)^T, \quad h_i^1 = h_i \cdot -j4\pi\frac{d_x}{\lambda R_0}\left\lceil\frac{i}{M}\right\rceil$$

$$\boldsymbol{\gamma}_1 = \boldsymbol{\gamma} \odot \text{vec}(\Delta x), \quad \Delta x = [\delta x_{p,q}]_{PQ} \tag{21}$$

where $\lceil \cdot \rceil$ denotes the ceiling function and $\odot$ denotes the Hadamard product. With the same procedure, the third term in

(20) can be rewritten as

$$\sum_{p=1}^{P}\sum_{q=1}^{Q}\gamma_{pq}\exp\left(j4\pi\left(\frac{x_m}{\lambda R_0}x_p + \frac{y_n}{\lambda R_0}y_q\right)\right)$$
$$\left(j4\pi\frac{y_n\delta y_{pq}}{\lambda R_0}\right) = \boldsymbol{H}_2(x, y)\boldsymbol{\gamma}_2$$

$$\boldsymbol{H}_2(x, y) = (h_1^2, h_2^2, \ldots, h_{MN}^2)^T, \quad h_i^2 = h_i \cdot j4\pi\frac{d_y}{\lambda R_0}\left\lceil\frac{i}{N}\right\rceil \tag{22}$$

$$\boldsymbol{\gamma}_2 = \boldsymbol{\gamma} \odot \text{vec}(\Delta y), \quad \Delta y = [\delta y_{p,q}]_{PQ}.$$

Then, the vectorization model of the 2-D mismatch compensation in DLLA 3-D SAR can be expressed as

$$\hat{s} = \boldsymbol{H}(x, y)\boldsymbol{\gamma} + \boldsymbol{H}_1(x, y)\boldsymbol{\gamma}_1 + \boldsymbol{H}_2(x, y)\boldsymbol{\gamma}_2 + n_0$$
$$= [\boldsymbol{H}(x, y), \boldsymbol{H}_1(x, y), \boldsymbol{H}_2(x, y)]\begin{bmatrix}\boldsymbol{\gamma}\\\boldsymbol{\gamma}_1\\\boldsymbol{\gamma}_2\end{bmatrix} + n_0 \tag{23}$$
$$= \boldsymbol{H}_0\boldsymbol{\gamma}_0 + n_0$$

where $\boldsymbol{H}_0 \in \mathbb{C}^{MN \times 3PQ}$ is the partitioned matrix that consists of $\boldsymbol{H}$, $\boldsymbol{H}_1$, and $\boldsymbol{H}_2$, $\boldsymbol{\gamma}_0 \in \mathbb{C}^{3PQ}$ contains the information of scattering coefficient and gridding error in the X–Y plane, and $n_0 = n + \boldsymbol{H}\boldsymbol{\gamma} \odot O(\delta^2)$ contains the noise and the high-order component of the gridding error. The specifical expression for the high-order component of the gridding error $\boldsymbol{H}\boldsymbol{\gamma} \odot O(\delta^2)$ is shown as the last term in (20). Suppose the grid interval is 1 m×1 m, and the imaging area is 100 m×100 m, since the gridding error is smaller than 1 m, the ratio of the high-order component and the principal component is $(1 + O(\delta))/O(\delta^2) \approx 40$ dB, which is higher than the signal-to-noise ratio in most cases. As a result, the high-order component of the gridding error can generally be ignored since the high-order component is smaller than the noise in most cases. Then, the 2-D mismatch compensation can be transformed into the optimization problem as follows:

$$\boldsymbol{\gamma}_0 = \arg\min_{\boldsymbol{\gamma}_0}\left\{\|\hat{s} - \boldsymbol{H}_0\boldsymbol{\gamma}_0\|_2^2 + \rho\|\boldsymbol{\gamma}_0\|_P\right\}, \quad 0 \le P \le 1 \tag{24}$$

which can be solved by the same algorithms with (11), i.e., the OGSBI algorithm.

C. Two-Dimensional Mismatch Compensation of Joint Model

In the above 2-D mismatch compensation model, the approximation of Taylor expression is chosen instead of the atomic norm minimization to reduce the cost of computation. However, the vectorization operation leads to a rapidly increasing size of the problem with higher imaging resolution and enhances the loads of storage and computation. Owing to the echo signal in (13) can be expressed as a joint matrix form

$$S = A(X)\boldsymbol{\Omega}B(Y) \tag{25}$$

where

$$A(X) = \begin{bmatrix} A_{11} & A_{12} & \cdots & A_{1P} \\ A_{21} & A_{22} & \cdots & A_{2P} \\ \vdots & \vdots & \ddots & \vdots \\ A_{M1} & A_{M2} & \cdots & A_{MP} \end{bmatrix},$$

$$A_{mp} = \exp\left(j4\pi \frac{x_m}{\lambda R_0} x_p\right),$$

$$B(Y) = \begin{bmatrix} B_{11} & B_{12} & \cdots & B_{1N} \\ B_{21} & B_{22} & \cdots & B_{2N} \\ \vdots & \vdots & \ddots & \vdots \\ B_{Q1} & B_{Q2} & \cdots & B_{QN} \end{bmatrix}, \quad B_{qn}$$

$$= \exp\left(j4\pi \frac{y_n}{\lambda R_0} y_q\right) \tag{26}$$

where $X = [x_1, x_2, \ldots, x_M]^T$, $x_m = [dx_1, \ldots, dx_p]^T$ denotes the location of uniform grids in the X-direction, and $Y = [y_1, y_2, \ldots, y_N]^T$, $y_m = [dy_1, \ldots, dy_p]^T$ denotes the location of uniform grids in the Y-direction, respectively. Correspondingly, the echo signal of (14) can be expressed as

$$\hat{S} = A(\hat{X})\boldsymbol{\Omega}B(\hat{Y}) \tag{27}$$

where $\hat{X}$ and $\hat{Y}$, respectively, denote the set of unbiased grid position in the X-direction and the Y-direction, and $\boldsymbol{\Omega}$ is the corrected scattering coefficient matrix. For one grid point located at (pdx, qdy), only one scatterer may locate in the range of $(\pm\frac{1}{2}dx, \pm\frac{1}{2}dy)$, and the location of the scatterer is denoted by $(\hat{x}_{pq}, \hat{y}_{pq})$. Then, the $\hat{X}$ and $\hat{Y}$ can be written as $\hat{X} = [\hat{x}_{pq}]_{P \times Q}$ and $\hat{Y} = [\hat{y}_{pq}]_{P \times Q}$. The grid error matrix of $\boldsymbol{\Omega}$ in the X-direction and Y-direction is denoted by ΔX and ΔY, respectively.

The following approach is to compensate for the 2-D mismatch problem by adjusting the grid positions $\hat{X}$ and $\hat{Y}$, which means that the corrected scattering coefficient matrix $\boldsymbol{\Omega}$ and the

gridding errors must be obtained to achieve the final imaging result. In (27), the gridding errors in the X-direction and Y-direction can be analyzed separately. If the signal before forced in the Y-direction is regarded as an entirety, which can be denoted as $\hat{S}_Y = \boldsymbol{\Omega}B(\hat{Y})$, the model can be expressed as

$$\hat{S} = A(\hat{X})\hat{S}_Y. \tag{28}$$

Suppose that the ith column of $\hat{S}_Y$ is denoted by $\hat{S}_{Yi}$, it can be expressed as $\hat{S}_Y = [\hat{S}_{Y1}, \hat{S}_{Y2}, \ldots, \hat{S}_{YM}]$. For each column of $\hat{S}$, the measurement matrix A and the mismatched part ΔX^s can be divided by Taylor expression

$$\hat{S}_i = A(\hat{X}_i)\hat{S}_{Yi} = \left(A(X) + \frac{A}{\partial X}\text{diag}(\Delta X_i^s)\right)\hat{S}_{Yi}$$

$$= \begin{bmatrix} A(X) & \frac{A}{\partial X} \end{bmatrix} \begin{bmatrix} \hat{S}_{Yi} \\ \Delta X_i^s \odot \hat{S}_{Yi} \end{bmatrix} \tag{29}$$

where $\hat{S}_i$ denotes the ith column of $\hat{S}$, ΔX_i^s is the matrix of mismatch parameters for $\hat{S}_{Yi}$, and $\text{diag}(\cdot)$ denotes the diagonalization operation. According to the theory of partitioned matrix, $\hat{\boldsymbol{S}}$ can be expressed as

$$\hat{S} = \begin{bmatrix} \hat{S}_1, \hat{S}_2, \ldots, \hat{S}_M \end{bmatrix}$$

$$= \begin{bmatrix} A(X) & \frac{A}{\partial X} \end{bmatrix} \begin{bmatrix} \hat{S}_{Y1} & \hat{S}_{Y2} & \cdots & \hat{S}_{YM} \\ \Delta X_1^s \odot \hat{S}_{Y1} & \Delta X_2^s \odot \hat{S}_{Y1} & \cdots & \Delta X_M^s \odot \hat{S}_{Y1} \end{bmatrix}$$

$$= \begin{bmatrix} A(X) & \frac{A}{\partial X} \end{bmatrix} \begin{bmatrix} \hat{S}_Y \\ \Delta X^s \odot \hat{S}_Y \end{bmatrix}. \tag{30}$$

It is notable that the $\Delta X^s \in \mathbb{C}^{M \times P}$ is the matrix of mismatch parameters for $\hat{S}_Y$ instead of $\boldsymbol{\Omega}$, which means that the ΔX_i^s is not real gridding error in the X-direction.

Suppose that the ith row of $\hat{S}_Y$ is denoted by $\hat{S}_Y^i$, it can be expressed as $\hat{S}_Y = [(\hat{S}_Y^1)^T, (\hat{S}_Y^2)^T, \ldots, (\hat{S}_Y^Q)^T]^T$; then, (27)

$$\hat{s} = \sum_{p=1}^{P}\sum_{q=1}^{Q} \gamma_{pq} \cdot \exp\left(j4\pi\left(\frac{x_m}{\lambda R_0}x_p + \frac{y_n}{\lambda R_0}y_q\right)\right)\left(1 + j4\pi\frac{x_m}{\lambda R_0}\delta x_{p,q} + j4\pi\frac{y_n}{\lambda R_0}\delta y_{p,q} + O\left(|\delta x_{p,q}|^2\right)\right.$$

$$\left. + O\left(|\delta y_{p,q}|^2\right) + O\left(|\delta x_{p,q}||\delta y_{p,q}|\right)\right)$$

$$= \sum_{p=1}^{P}\sum_{q=1}^{Q} \gamma_{pq} \cdot \exp\left(j4\pi\left(\frac{x_m}{\lambda R_0}x_p + \frac{y_n}{\lambda R_0}y_q\right)\right) + \sum_{p=1}^{P}\sum_{q=1}^{Q} \gamma_{pq} \cdot \exp\left(j4\pi\left(\frac{x_m}{\lambda R_0}x_p + \frac{y_n}{\lambda R_0}y_q\right)\right)\left(j4\pi\frac{x_m}{\lambda R_0}\delta x_{p,q}\right)$$

$$+ \sum_{p=1}^{P}\sum_{q=1}^{Q} \gamma_{pq} \cdot \exp\left(j4\pi\left(\frac{x_m}{\lambda R_0}x_p + \frac{y_n}{\lambda R_0}y_q\right)\right)\left(j4\pi\frac{y_n}{\lambda R_0}\delta y_{p,q}\right)$$

$$+ \sum_{p=1}^{P}\sum_{q=1}^{Q} \gamma_{pq} \cdot \exp\left(j4\pi\left(\frac{x_m}{\lambda R_0}x_p + \frac{y_n}{\lambda R_0}y_q\right)\right) \cdot O\left(|\delta_{p,q}|^2\right)$$

$$O\left(|\delta_{p,q}|^2\right) = \left(\left(j4\pi\frac{x_m}{\lambda R_0}\right)^2(\delta x_{p,q})^2 + \left(j4\pi\frac{y_n}{\lambda R_0}\right)^2(\delta y_{p,q})^2 + \left(j4\pi\frac{y_n}{\lambda R_0}\right)\left(j4\pi\frac{x_m}{\lambda R_0}\right)(\delta x_{p,q})(\delta y_{p,q})\right) \tag{20}$$

can be further expressed as

$$\hat{S} = \begin{bmatrix} A(X) & \frac{A}{\partial X} \end{bmatrix} \begin{bmatrix} [(\hat{S}_Y^1)^T (\hat{S}_Y^2)^T \cdots (\hat{S}_Y^Q)^T]^T \\ \Delta X^s \odot [(\hat{S}_Y^1)^T (\hat{S}_Y^2)^T \cdots (\hat{S}_Y^Q)^T]^T \end{bmatrix}. \tag{31}$$

For further analysis, each row of $\hat{S}_Y$ can be decomposed as

$$\hat{S}_Y^i = \mathbf{\Omega}^i B(\hat{Y}_i) = \mathbf{\Omega}^i \left(B(Y) + \mathrm{diag}(\Delta Y_i)\frac{B}{\partial Y} \right)$$
$$= \begin{bmatrix} \mathbf{\Omega}^i & \mathbf{\Omega}^i \odot \Delta Y_i \end{bmatrix} \begin{bmatrix} B(Y) \\ \frac{B}{\partial Y} \end{bmatrix} \tag{32}$$

where $\mathbf{\Omega}^i$ denotes the ith row of $\mathbf{\Omega}$, and $\hat{Y}_i$ and ΔY_i, respectively, denote the corrected grid positions and the mismatch to the uniform grids for the ith row. According to (32), (31) can be expressed as

$$\hat{S} = \begin{bmatrix} A(X) & \frac{A}{\partial X} \end{bmatrix} \begin{bmatrix} \begin{bmatrix} \mathbf{\Omega}^1 & \mathbf{\Omega}^1 \odot \Delta Y_1 \\ \vdots & \vdots \\ \mathbf{\Omega}^Q & \mathbf{\Omega}^Q \odot \Delta Y_Q \end{bmatrix} \begin{bmatrix} B(Y) \\ \frac{B}{\partial Y} \end{bmatrix} \\ \Delta X^s \odot \left(\begin{bmatrix} \mathbf{\Omega}^1 & \mathbf{\Omega}^1 \odot \Delta Y_1 \\ \vdots & \vdots \\ \mathbf{\Omega}^Q & \mathbf{\Omega}^Q \odot \Delta Y_Q \end{bmatrix} \begin{bmatrix} B(Y) \\ \frac{B}{\partial Y} \end{bmatrix} \right) \end{bmatrix}. \tag{33}$$

Since the scattering coefficient matrix is $\mathbf{\Omega} = [(\mathbf{\Omega}^1)^T, \ldots, (\mathbf{\Omega}^Q)^T]^T$, (33) can be simplified as

$$\hat{S} = \begin{bmatrix} A(X) & \frac{A}{\partial X} \end{bmatrix}$$
$$\begin{bmatrix} \begin{bmatrix} \mathbf{\Omega} & \mathbf{\Omega} \odot \Delta Y \end{bmatrix} \begin{bmatrix} B(Y) \\ \frac{B}{\partial Y} \end{bmatrix} \\ \Delta X^s \odot \left(\begin{bmatrix} \mathbf{\Omega} & \mathbf{\Omega} \odot \Delta Y \end{bmatrix} \begin{bmatrix} B(Y) \\ \frac{B}{\partial Y} \end{bmatrix} \right) \end{bmatrix}. \tag{34}$$

$\Delta Y \in \mathbb{C}^{P \times Q}$ is the matrix of mismatch parameters for $\mathbf{\Omega}$, which means that ΔY is the real gridding error in the Y-direction. Because the Hadamard product $\odot$ and the matrix product are not satisfied with the associative law between each other, we have to define the matrix T_Y as

$$T_Y = \left(\Delta X^s \odot \left(\begin{bmatrix} \mathbf{\Omega} & \mathbf{\Omega} \odot \Delta Y \end{bmatrix} \begin{bmatrix} B(Y) \\ \frac{B}{\partial Y} \end{bmatrix} \right) \right) \begin{bmatrix} B(Y) \\ \frac{B}{\partial Y} \end{bmatrix}^{-1}. \tag{35}$$

Then, (34) can be further expressed as

$$\hat{S} = \begin{bmatrix} A(X) & \frac{A}{\partial X} \end{bmatrix} \begin{bmatrix} \begin{bmatrix} \mathbf{\Omega} & \mathbf{\Omega} \odot \Delta Y \end{bmatrix} \\ T_Y \end{bmatrix} \begin{bmatrix} B(Y) \\ \frac{B}{\partial Y} \end{bmatrix}. \tag{36}$$

Then, the corrected scattering coefficient matrix $\mathbf{\Omega}$ and gridding errors in the Y-direction ΔY can be obtained by solving (36).

However, the explicit representation of gridding errors in the X-direction is contained in the matrix U because the signal before forced in the Y-direction is first regarded as an entirety. If the signal before forced in the X-direction is regarded as an entirety $\hat{S}_X^T = A(\hat{X})\mathbf{\Omega}$, then (24) should be rewritten as

$$\hat{S}^T = B(\hat{Y})^T \mathbf{\Omega}^T A(\hat{X})^T = B(\hat{Y})^T \hat{S}_X. \tag{37}$$

For each column of $\hat{S}_X^T$, the measurement matrix B^T and the mismatched part ΔY^s can be divided by Taylor expression

$$\hat{S}_i^T = B(\hat{Y}_i)^T \hat{S}_{Xi} = \left(B(Y)^T + \frac{B^T}{\partial Y}\mathrm{diag}(\Delta Y_i) \right) \hat{S}_{Xi}$$
$$= \begin{bmatrix} B(Y)^T & \frac{B^T}{\partial Y} \end{bmatrix} \begin{bmatrix} \hat{S}_{Xi} \\ \Delta Y_i^s \odot \hat{S}_{Xi} \end{bmatrix} \tag{38}$$

where ΔX_i^s is the matrix of mismatch parameters for $\hat{S}_{Xi}$. Since $\hat{S}^T$ consists of N columns, it can be expressed as

$$\hat{S}^T = \begin{bmatrix} \hat{S}_1^T, \hat{S}_2^T, \ldots, \hat{S}_N^T \end{bmatrix}$$
$$= \begin{bmatrix} B(Y)^T & \frac{B^T}{\partial Y} \end{bmatrix} \begin{bmatrix} \hat{S}_{X1} \cdots \hat{S}_{XN} \\ \Delta Y_1^s \odot \hat{S}_{X1} \cdots \Delta Y_N^s \odot \hat{S}_{XN} \end{bmatrix}$$
$$= \begin{bmatrix} B(Y)^T & \frac{B^T}{\partial Y} \end{bmatrix} \begin{bmatrix} \hat{S}_X \\ \Delta Y^s \odot \hat{S}_X \end{bmatrix}. \tag{39}$$

It is notable that the $\Delta Y^s \in \mathbb{C}^{Q \times N}$ is the matrix of mismatch parameters for $\hat{S}_X$ instead of $\mathbf{\Omega}$, which means that the ΔY_i^s is not the real gridding error in the Y-direction.

As the ith row of $\hat{S}_X$ can be decomposed as

$$\hat{S}_X^i = \mathbf{\Omega}^{Ti} A(\hat{X}_i)^T = \mathbf{\Omega}^{Ti} \left(A(X) + \mathrm{diag}(\Delta X_i)\frac{A}{\partial X} \right)$$
$$= \begin{bmatrix} \mathbf{\Omega}^{Ti} & \mathbf{\Omega}^{Ti} \odot \Delta X_i \end{bmatrix} \begin{bmatrix} A(X) \\ \frac{A}{\partial X} \end{bmatrix}. \tag{40}$$

The matrix $\hat{S}_X$ can be expressed as

$$\hat{S}_X = \begin{bmatrix} \mathbf{\Omega}^T & \mathbf{\Omega}^T \odot \Delta \mathbf{X} \end{bmatrix} \begin{bmatrix} A(X)^T \\ \frac{A^T}{\partial X} \end{bmatrix}. \tag{41}$$

$\Delta X \in \mathbb{C}^{P \times Q}$ is the matrix of mismatch parameters for $\mathbf{\Omega}$, which means that ΔX is the real gridding error in the X-direction. According to (39) and (41), $\hat{S}^T$ can be expressed as

$$\hat{S}^T = \begin{bmatrix} B(Y)^T & \frac{B^T}{\partial Y} \end{bmatrix}$$
$$\begin{bmatrix} \begin{bmatrix} \mathbf{\Omega}^T & \mathbf{\Omega}^T \odot \Delta X \end{bmatrix} \begin{bmatrix} A(X)^T \\ \frac{A^T}{\partial X} \end{bmatrix} \\ \Delta Y^s \odot \left(\begin{bmatrix} \mathbf{\Omega}^T & \mathbf{\Omega}^T \odot \Delta X \end{bmatrix} \begin{bmatrix} A(X)^T \\ \frac{A^T}{\partial X} \end{bmatrix} \right) \end{bmatrix}. \tag{42}$$

To further simplify (42), we define the matrix T_X as

$$T_X =$$
$$\left(\Delta Y^s \odot \left(\begin{bmatrix} \mathbf{\Omega}^T & \mathbf{\Omega}^T \odot \Delta X \end{bmatrix} \begin{bmatrix} A(X)^T \\ \frac{A^T}{\partial X} \end{bmatrix} \right) \right) \begin{bmatrix} A(X)^T \\ \frac{A^T}{\partial X} \end{bmatrix}^{-1}. \tag{43}$$

Then, (42) can be expressed as

$$\hat{S}^T = \begin{bmatrix} B(Y)^T & \frac{B^T}{\partial Y} \end{bmatrix} \begin{bmatrix} \mathbf{\Omega}^T & \mathbf{\Omega}^T \odot \Delta X \\ T_X \end{bmatrix} \begin{bmatrix} A(X)^T \\ \frac{A^T}{\partial X} \end{bmatrix}. \tag{44}$$

According to (36) and (44), the equation is established as

$$\begin{bmatrix} \begin{bmatrix} \mathbf{\Omega} & \mathbf{\Omega} \odot \Delta Y \end{bmatrix} \\ T_Y \end{bmatrix} = \begin{bmatrix} \mathbf{\Omega}^T & \mathbf{\Omega}^T \odot \Delta X \\ T_X \end{bmatrix}^T. \tag{45}$$

Since (36) and (44) are symmetric with each other, if we divide T_Y and T_X as $T_Y = [T_{Y1}, T_{Y2}]$, $T_{Y1}, T_{Y2} \in \mathbb{C}^{Q \times P}$, and $T_X = [T_{X1}, T_{X2}]$, $T_{X1}, T_{X2} \in \mathbb{C}^{P \times Q}$, the explicit representation of gridding errors in T_Y and T_X can be obtained as

$$\begin{cases} T_{Y1} = \mathbf{\Omega} \odot \Delta X^T \\ T_{X1} = \mathbf{\Omega}^T \odot \Delta Y^T \\ T_{Y2} = T_{X2}^T \end{cases}. \tag{46}$$

Then, the joint model of the 2-D mismatch compensation can be simplified as

$$\hat{S} = \mathbf{\Phi}_x \tilde{\mathbf{\Omega}} \mathbf{\Phi}_y \tag{47}$$

where $\mathbf{\Phi}_x = [\, A(X) \; \frac{A}{\partial X} \,]$ and $\mathbf{\Phi}_y = [\, B(Y) \; \frac{B}{\partial Y} \,]^T$ denote the corrected basis matrices in the azimuth and cross-track direction, respectively, and $\tilde{\mathbf{\Omega}} = [\, {}^{\mathbf{\Omega}}_{\mathbf{\Omega} \odot \Delta X^T} \; {}^{\mathbf{\Omega} \odot \Delta Y}_{T_{Y2}} \,]$. If we can achieve $\tilde{\mathbf{\Omega}}$ from (47), the 2-D mismatch in DLLA 3-D SAR can be compensated by the corrected scattering coefficient matrix $\mathbf{\Omega}$, gridding errors in the X-direction ΔX, and gridding errors in the Y-direction ΔY. Recalling the vectorization processing method in Section III-B, the 1-D vector form in (23) has been converted into the above 2-D reconstruction problem. It is clear that the size of (23), including $\mathbf{H}_0 \in \mathbb{C}^{MN \times 3PQ}$ and $\gamma_0 \in \mathbb{C}^{3PQ}$ with $3(MN + 1)PQ$ elements, is much larger than the size of (47), including $\mathbf{\Phi}_x \in \mathbb{C}^{M \times 2P}$, $\mathbf{\Phi}_y \in \mathbb{C}^{2Q \times N}$, and $\tilde{\mathbf{\Omega}} \in \mathbb{C}^{2P \times 2Q}$ with $2NQ + 2MP + 4PQ$ elements. Therefore, the model of (47) can save a lot of computing memory compared with vectorization processing in (23).

D. Algorithm for the 2-D Mismatch Compensation

As we know, the sparse recovery problem in (45) is underdetermined when $N < Q$ and $M < P$. In the presence of the noise, the sparse matrix $\tilde{\mathbf{\Omega}}$ can be recovered by minimizing the l_0-norm of $\tilde{\mathbf{\Omega}}$

$$\min \left\| \tilde{\mathbf{\Omega}} \right\|_0 \text{s.t.} \left\| \hat{S} - \mathbf{\Phi}_x \tilde{\mathbf{\Omega}} \mathbf{\Phi}_y \right\|_2^2 < \varepsilon \tag{48}$$

where $\| \cdot \|_2$ denotes the 2-D norm of a matrix, and ε is related to the noise variance.

According to the derivation from (27) to (48), the 2-D joint model with 2-D mismatch is transformed to a normal sparse linear model, which is suitable for most of the CS reconstruction algorithms. Among many 2-D CS algorithms improved by the corresponding 1-D CS reconstruction algorithms, such as 2-D SL0, 2-D SBL, and 2-D iterative adaptive approach [34], the 2-D SL0 algorithm is chosen to enhance the computational efficiency. Here is a brief introduction to the theory of the 2-D SL0 algorithm and the detailed procedure is shown in [34]. To approximate the l_0-norm, which is a discontinuous function, the 2-D SL0 algorithm utilizes a continuous Gaussian function as

$$\left\| \tilde{\mathbf{\Omega}} \right\|_0 \approx 4PQ - F_\sigma(\tilde{\mathbf{\Omega}}), \quad \sigma \to 0, \quad F_\sigma(\tilde{\mathbf{\Omega}})$$

$$= \sum_{p=1}^{2P} \sum_{q=1}^{2Q} \exp\left(-\frac{|\gamma_{p,q}|}{2\sigma^2} \right). \tag{49}$$

Algorithm 1: MOGSL0 for DLLA 3-D SAR Imaging.

Input: 3-D signal $\hat{S}_0$; measurement matrices $\mathbf{\Phi}_x$ and $\mathbf{\Phi}_y$;
Output: Scattering coefficient matrix $\mathbf{\Omega}$; gridding errors in the X-direction ΔX; gridding errors in the Y-direction ΔY;
Step 1: Range Compression
1) Transform $\hat{S}_0$ to frequency domain: $\hat{F}_0 = \text{FT}_r(\hat{S}_0)$
2) Matched filter and range migration correction:
   $\hat{F}_r = \hat{F}_0 \cdot H_r \cdot H_{\text{rma}} \cdot H_{\text{rmc}}$
3) Transform $\hat{F}_r$ to time domain: $\hat{S}_r = \text{IFT}_r(\hat{F}_r)$
4) Deramping operation: $\hat{S} = \hat{S}_r \cdot H_{\text{der}}$
5) Divide $\hat{S}$ into a series of the 2-D matrix for each range cell: $\hat{S} = [\hat{S}^1, \hat{S}^2, \ldots, \hat{S}^{Nr}]$
Step 2: 2-D mismatch compensation via 2-D SL0
For $i \in [1, N_r]$ **do**
Let $\tilde{\mathbf{\Omega}}_0 = \mathbf{\Phi}_x^+ \hat{S}^i \mathbf{\Phi}_y^+$
Set a sequence as $\sigma = \{\sigma_1, \sigma_2, \ldots, \sigma_J\}, \quad \sigma_j = c_0 \sigma_{j-1}$,
   where $c_0 \in (0, 1)$ is a constant.
For $j \in [1, J]$ **do**
Let $\sigma = \sigma_j$ and $\tilde{\mathbf{\Omega}} = \tilde{\mathbf{\Omega}}_{j-1}$
For $l \in [1, L]$ **do**
Let $\nabla F_\sigma(\tilde{\mathbf{\Omega}}) = [\delta_{p,q}]_{2P \times 2Q}$, where
   $\delta_{p,q} = \exp(-|\gamma_{p,q}|/2\sigma^2)$,
Let $\tilde{\mathbf{\Omega}}' = \tilde{\mathbf{\Omega}} - \mu \nabla F_\sigma(\tilde{\mathbf{\Omega}})$, where $\mu \geq 1$ is a constant.
Obtain the backward projection of $\tilde{\mathbf{\Omega}}$ on the feasible set:
$\tilde{\mathbf{\Omega}} = \tilde{\mathbf{\Omega}}' - \mathbf{\Phi}_x^+ (\mathbf{\Phi}_x \tilde{\mathbf{\Omega}}' \mathbf{\Phi}_y - \hat{S}^i) \mathbf{\Phi}_y^+$,
where $\mathbf{\Phi}_x^+ = \mathbf{\Phi}_x^T (\mathbf{\Phi}_x \mathbf{\Phi}_x^T)^{-1}$ and $\mathbf{\Phi}_y^+ = \mathbf{\Phi}_y^T (\mathbf{\Phi}_y \mathbf{\Phi}_y^T)^{-1}$
   are the pseudoinverse of $\mathbf{\Phi}_x$ and $\mathbf{\Phi}_y$.
end for
Set $\tilde{\mathbf{\Omega}}_j = \tilde{\mathbf{\Omega}}$.
end for
Set $\mathbf{\Omega}^i = \tilde{\mathbf{\Omega}}_J(1 : P, 1 : Q)$ and
   $\Delta Y^i = \tilde{\mathbf{\Omega}}^i(1 : P, Q + 1 : 2Q) \odot W^i$, where W^i is the reciprocal matrix of $\mathbf{\Omega}^i$.
end for
Set $\mathbf{\Omega} = [\mathbf{\Omega}^1, \mathbf{\Omega}^2, \ldots, \mathbf{\Omega}^{Nr}]$,
   $\Delta X = [\Delta X^1, \Delta X^2, \ldots, \Delta X^{Nr}]$, and
   $\Delta Y = [\Delta Y^1, \Delta Y^2, \ldots, \Delta Y^{Nr}]$.

When σ is small enough, the maximization of $F_\sigma(\tilde{\mathbf{\Omega}})$ is equal to the minimization of the l_0-norm of $\tilde{\mathbf{\Omega}}$. A decreasing sequence of σ is utilized to obtain the global maximum of $F_\sigma(\tilde{\mathbf{\Omega}})$ instead of the local maxima and the steepest ascent method is used to maximize $F_\sigma(\tilde{\mathbf{\Omega}})$ for each σ.

Since (47) is a joint model with 2-D mismatch compensation, the proposed matrix-processed off-grid SL0 (MOGSL0) algorithm for DLLA 3-D SAR imaging is described in Algorithm 1.

V. EXPERIMENTS

In this section, the simulation experiments are carried out to verify the proposed algorithm. Point targets and distributed scene are provided to evaluate the effectiveness. The system parameters of DLLA 3-D SAR are listed in Table I.

TABLE I
SIMULATION PARAMETERS

parameter	value	parameter	value
Center Wavelength	8 mm	Signal Bandwidth	300 MHz
Signal Pulse Width	4 us	A/D Sampling Frequency	360 MHz
Range Sampling Number	1600	Platform Flying Height	1000 m
AT[1] Sampling Number	256	CT[2] Sampling Number	256
AT Sampling Interval	0.01 m	CT Sampling Interval	0.01 m
AT Beam Width	14°	CT Beam Width	14°

[1] AT is short for along-track; [2] CT is short for cross-track.
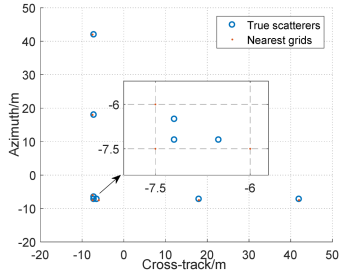
Fig. 3.   Off-grid scatterers in a range cell.

A. Reconstruction Performance for Off-Grid Scatterers

For a practical imaging scene, usually, more than one off-grid scatterer is in the same range cell. In the first experiment, we assume that there are seven scatterers in a range cell to compare the reconstruction performance of different methods. The locations of the seven off-grid scatterers are shown in Fig. 3. Orthogonal matching pursuit (OMP) is based on the vectorization model without mismatch compensation, the 2-D SL0 is based on the joint model without mismatch compensation, and OGSBI is based on the vectorization model with mismatch compensation. We compare the proposed MOGSL0 method with the above three methods on both reconstruction performance and the time cost. The parameters of MOGSL0 are $\sigma_1 = 4 \max |\tilde{\Omega}_0|$, $c_0 = 0.5$, $L = 5$, and $\mu = 2$, which is the general setting of SL0 algorithms [34]. Since the azimuth and the cross-track Rayleigh resolution [21] are both about 1.5 m according to the system parameters, the grid intervals d_x and d_y for imaging are equal to the Rayleigh resolution. Fig. 4 shows the results under two different SNRs, and for display clear, the azimuth and cross-track profile of the reconstructed scatterers is given.

As shown in Fig. 4(a) and (b), when the SNR is low as 5 dB, all the methods cannot give the accurate reconstruction since the measurement noise dominates the uncertainties. When SNR increases to 25 dB, the proposed method and OGSBI can reconstruct all scatterers accurately, while the method OMP and 2-D SL0 still suffer from spurious estimation for the off-grid scatterers and tend to miss the weak scatterer or the close scatterers. Furthermore, the mean square error (MSE) of the location estimation via 100 Monte Carlo trials is shown in
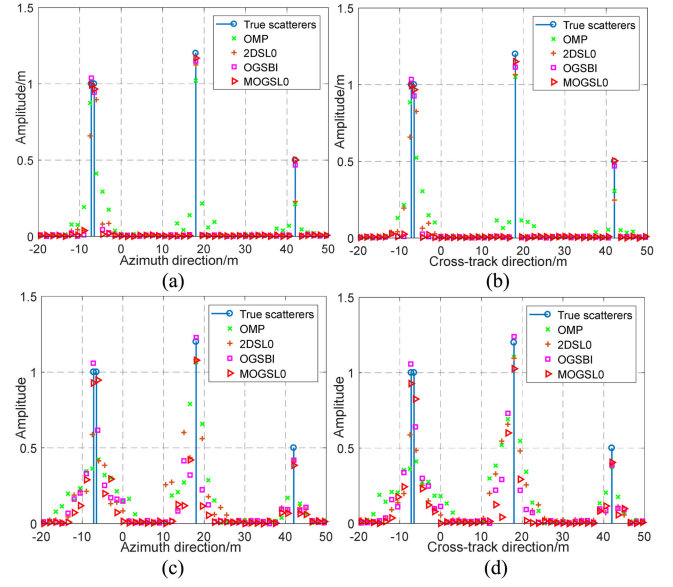

Fig. 4.   Cross-track profile and azimuth profile of reconstruction result in different SNRs. (a) Cross-track profile with SNR = 25 dB. (b) Azimuth profile with SNR = 25 dB. (c) Cross-track profile with SNR = 5 dB. (d) Azimuth profile with SNR = 5 dB.
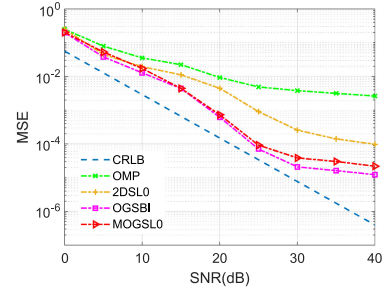

Fig. 5.   Reconstruction performance for off-grid scatterers by MSE versus SNR.

Fig. 5 to quantize the performance under different SNRs. The Cramer–Rao lower bound (CRLB) in white Gaussian noise of a single scatterer location is asymptotical [2], [25]

$$\text{CRLB}(x) = \frac{3}{2\pi^2} \frac{\rho_x^2}{\text{SNR}} \tag{50}$$

which is a common benchmark to evaluate the performance. Since the azimuth dimension and the cross-track dimension are totally symmetric, Fig. 5 only shows the MSE of cross-track reconstruction. When SNR is low, all the methods have high errors. When SNR becomes larger, all the methods have lower errors, but the proposed method still has a better performance than OMP and SL0, which still suffer from the off-grid effect. Since the OGSBI is based on the Bayesian estimation, which performs surprisingly accurate results as the noise distribution is known, the MSE of OGSBI is better than the proposed MOGSL0 method.

To compare the computational complexity of the methods, we recall the azimuth sampling number M, the cross-track sampling

TABLE II
COMPUTATIONAL COMPLEXITY

	computational complexity		computational complexity
MOGSL0	$O((M+N) \times 3PQ)$	2-D SL0	$O((M+N) \times PQ)$
OGSBI	$O((MN)^2 \times 3PQ)$	OMP	$O(MN \times PQ \times K)$

TABLE III
RELATIVE ERROR

	Region I	Region II	Region III	Region IV	Running time
MOGSL0	0.24	0.16	0.39	0.30	72.24s
OGSBI	0.41	0.19	0.45	0.37	1193.85s
2-D SL0	0.35	0.27	0.67	0.43	23.76s
OMP	0.46	0.31	0.74	0.48	129.51s
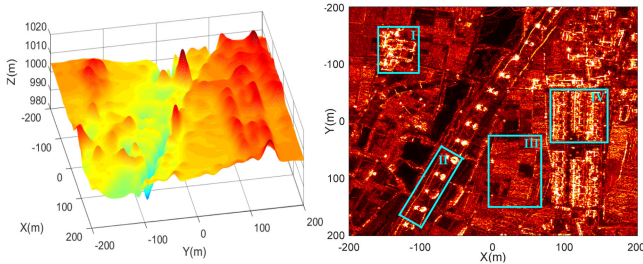
Fig. 6. Three-dimensional distributed scene. (a) DEM. (b) Circular SAR image.

number N, the azimuth gridding number P, the cross-track gridding number Q, and the scatterer number K, and the relation is $K < M, N \leq P, Q$. As given in Table II, the computational complexity of OMP is about $O(MN \times PQ \times K)$, and the OGSBI has a computational complexity of $O((MN)^2 \times 3PQ)$ per iteration. The 2-D SL0 and MOGSL0 have a computational complexity of $O((M+N) \times PQ)$ and $O((M+N) \times 3PQ)$ per iteration, respectively. Since the iteration times of SL0 are constant, the computational complexities of MOGSL0 and 2-D SL0 increase slower than that of the other two methods. In the above simulation experiments, MOGSL0, OGSBI, SL0, and OMP take about 0.0451, 0.7439, 0.0137, and 0.0796 s, respectively.

B. Experiment for Distributed Extended Targets

To validate the proposed method further, an airborne CSAR SAR image and the corresponding DEM data are chosen for the 3-D distributed scene reconstruction. The simulated DLLA 3-D SAR data generation needs the position of scatterers and the coefficient of scatterers, which are from DEM data and a SAR image for the same region, respectively. As shown in Fig. 6, the elevation locations and the coefficients of the scatterers are provided by the DEM data and the circular SAR image. The SAR image can also be obtained by any kind of SAR only if it is for the

same region as the DEM data. Coincidentally, this SAR image is obtained by an airborne CSAR. This data generation mode for DLLA 3-D SAR has been widely used to verify the imaging performance of the distributed extended targets [26]–[28], [30]. At first, the scatterers distribute uniformly in the azimuth direction and cross-track direction with 1 m interval, which is less than the azimuth and cross-track Rayleigh resolution 1.5 m. To represent the off-grid scatterers, 20% random deviation from the uniform interval is added into the azimuth coordinate (*X*-direction) and the cross-track coordinate (*Y*-direction) of scatterers. As the grid intervals d_x and d_y for imaging are chosen to match the Rayleigh resolution, the off-grid scatterers exist in the simulated scene. Before imaging, white Gaussian noise is added to the echo signal and the SNR is chosen as 25 dB.

Fig. 7(a) and (c) shows the 3-D reconstructed images obtained by the azimuth and cross-track joint reconstruction via 2-D SL0 [12] and MOGSL0. Fig. 7(b) and (d) shows the 3-D reconstructed images obtained by the cross-track reconstruction via OGSBI [30] and OMP, respectively. Fig. 7(e)–(h) shows the orthogonal projection images onto the *X*--*Y* plane by the four methods. Fig. 7(i)–(l) shows the 3-D reconstructed point cloud colored by the height of MOGSL0, OGSBI, 2-D SL0, and OMP, respectively. The 3-D reconstructed point clouds are colored by the height of the reconstructed results. For the two methods, BCS and 2-D SL0, without compensating the mismatch problem caused by the off-grid scatterers, the corresponding reconstructed results contain many spurious scatterers and many image details are lost. In contrast, better image contrast and more details are provided by the proposed MOGSL0 and OGSBI, which compensate the mismatch problem.

Since the coefficients of the scatterers are provided by the circular SAR image in Fig. 6(b), the scattering coefficients distribution of the reconstructed images should be close to that of the input 2-D SAR image. The grayscale histograms of the input 2-D image and the orthographic projection images reconstructed by MOGSL0, OGSBI, 2-D SL0, and BCS are illustrated in Fig. 8. Compared with MOGSL0 and OGSBI, the histograms of the orthographic projection images obtained by the 2-D SL0 and BCS have a larger offset than that of the original input image. And the dynamic ranges of 2-D SL0 and BCS are smaller than that of MOGSL0 and OGSBI, which can also indicate that the reconstructed images obtained by the 2-D SL0 and BCS lose image details.

To quantify the reconstructed position accuracy, the relative error of both azimuth and cross-track positions is defined as $\frac{1}{k} \sum_{k=1}^{N_p N_q} (\|\hat{x}_k - x_k\|_2 + \|\hat{y}_k - y_k\|_2)/(\|x_k\|_2 + \|y_k\|_2)$, where $N_p N_q$ is the scatter number. The relative error between the reconstructed position values and the true position values of the regions I–IV marked in Fig. 6(b) is given in Table III. Compared with the methods without compensating the mismatch problem, MOGSL0 and OGSBI have smaller reconstruction errors, especially for region III, which is the region with weak scattering coefficients. Moreover, the total running time is given in Table III. The 3-D reconstructed results of MOGSL0 and 2-D SL0 have a shorter running time than OGSBI and OMP, which can indicate the advantages of matrix processing.
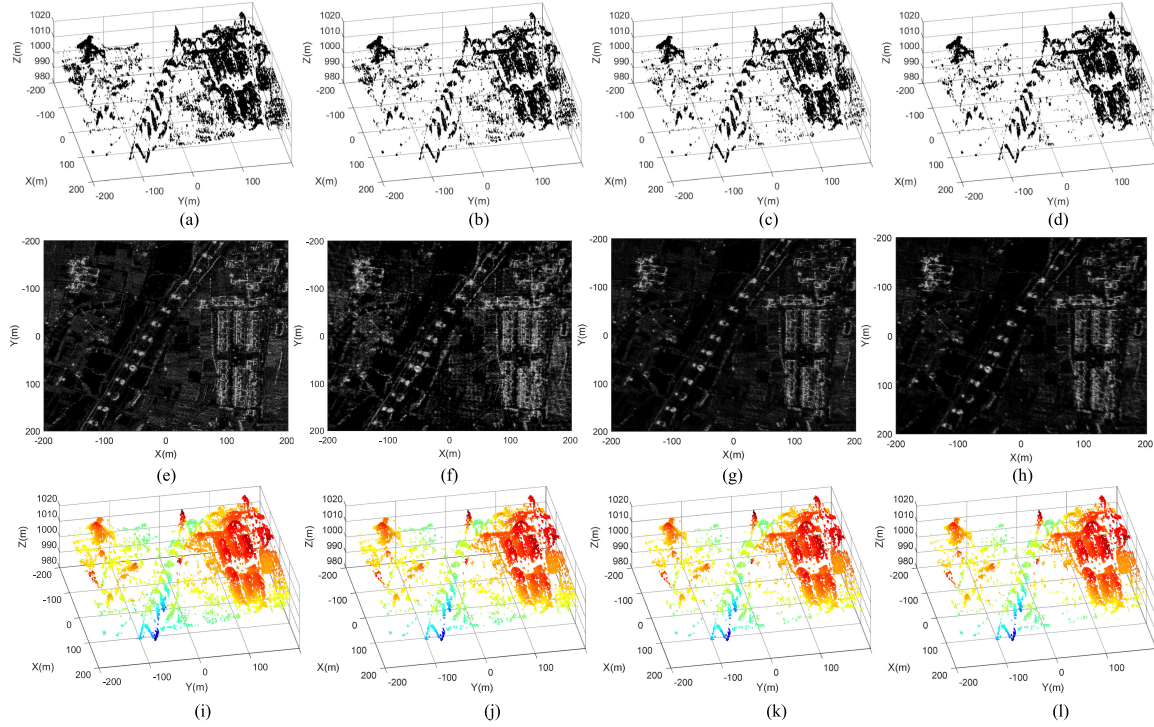
Fig. 7. Three-dimensional reconstructed image of (a) MOGSL0, (b) OGSBI, (c) 2-D SL0, and (d) OMP. The *X*--*Y* plane projection image of (e) MOGSL0, (f) OGSBI, (g) 2-D SL0, and (h) OMP. The 3-D reconstructed point cloud colored by the height of (i) MOGSL0, (j) OGSBI, (k) 2-DSL0, and (l) OMP.
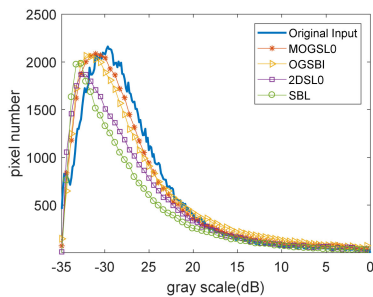

Fig. 8. Grayscale histogram comparison of the input 2-D image and the orthographic projection images reconstructed by MOGSL0, OGSBI, 2-D SL0, and BCS.

VI. CONCLUSION

In this article, a novel DLLA 3-D SAR imaging method based on the 2-D mismatch compensation is proposed. Instead of converting the 2-D matrix signals to the 1-D vectors, the proposed method directly compensates the 2-D mismatch with the 2-D joint model. Furthermore, the 2-D joint model with the 2-D mismatch is transformed into a normal sparse linear model, which is suitable for most of the CS reconstruction algorithms. It can provide better reconstruction performance and reduce the size of the problem. Finally, simulation experiments are shown to demonstrate the validity of the proposed method.

ACKNOWLEDGMENT

REFERENCES

[1] M. Soumekh, *Synthetic Aperture Radar Signal Processing With MATLAB Algorithms*. New York, NY, USA: Wiley, 1999.

[2] C. Ding, X. Qiu, F. Xu, X. Liang, Z. Jiao, and F. Zhang, "Synthetic aperture radar three-dimensional imaging—From TomoSAR and array InSAR to microwave vision," *J. Radars*, vol. 8, pp. 693–709, 2019.

[3] E. Aguilera, M. Nannini, and A. Reigber, "Wavelet-based compressed sensing for SAR tomography of forested areas," *IEEE Trans. Geosci. Remote Sens.* vol. 51, no. 12, pp. 5283–5295, Dec. 2013.

[4] Y. Lin, W. Hong, W. Tan, M. Xiang, and Y. Wang, "Airborne circular SAR imaging: Results at P-band," in *Proc. IEEE Int. Geosci. Remote Sens. Symp.*, Munich, Germany, Jul. 2012, pp. 5594–5597.

[5] C. H. Gierull, "On a concept for an airborne downward-looking imaging radar," *AEU Int. J. Electron. Commun.*, vol. 53, no. 6, pp. 295–304, 1999.

[6] J. Nouvel, H. Jeuland, G. Bonin, O. Du Plessis, J. Peyret, and S. Roques, "A Ka band imaging radar: DRIVE on board ONERA motorglider," in *Proc. IEEE Int. Symp. Geosci. Remote Sens.*, Denver, CO, USA, Aug. 2006, pp. 134–136.

[7] J. Klare, M. Weiss, O. Peters, A. Brenner, and J. Ender, "ARTINO: A new high resolution 3-D imaging radar system on an autonomous airborne platform," in *Proc. IEEE Int. Symp. Geosci. Remote Sens.*, Denver, CO, USA, Aug. 2006, pp. 3842–3845.

[8] Z. Donghao and Z. Xiaoling, "Downward-looking 3-D linear array SAR imaging based on chirp scaling algorithm," in *Proc. 2nd Asian-Pac. Conf. Synthetic Aperture Radar*, Oct. 2009, pp. 1043–1046.

[9] L. Du, Y. Wang, W. Tan, Y. Wu, and W. Hong, "A three-dimensional range migration algorithm for downward-looking 3D-SAR with single-transmitting and multiple-receiving linear array antennas," *EURASIP J. Adv. Signal Process.*, vol. 2010, 2010, Art. no. 957916.

[10] X. Peng, W. Tan, Y. Wang, W. Hong, and Y. Wu, "Convolution back-projection imaging algorithm for downward-looking sparse linear array three dimensional synthetic aperture radar," *Prog. Electromagn. Res.*, vol. 129, pp. 287–313, Sep. 2012.

[11] X. Peng, W. Hong, W. Tan, Y. Wu, and Y. Wang, "Polar format imaging algorithm with wave-front curvature phase error compensation for airborne DLSLA three-dimensional SAR," *IEEE Geosci. Remote Sens. Lett.*, vol. 11, no. 6, pp. 1036–1040, Jun. 2014.

[12] S. Zhang, G. Dong, and G. Kuang, "Superresolution downward-looking linear array three-dimensional SAR imaging based on two-dimensional compressive sensing," *IEEE J. Sel. Topics Appl. Earth Observ. Remote Sens.*, vol. 9, no. 6, pp. 2184–2196, Jun. 2016.

[13] S. Zhang, G. Dong, and G. Kuang, "Matrix completion for downward-looking 3-D SAR imaging with a random sparse linear array," *IEEE Trans. Geosci. Remote Sens.*, vol. 56, no. 4, pp. 1994–2006, Apr. 2018.

[14] S. R. DeGraaf, "SAR imaging via modern 2-D spectral estimation methods," *IEEE Trans. Image Process.*, vol. 7, no. 5, pp. 729–761, May 1998.

[15] D. L. Donoho, "Compressed sensing," *IEEE Trans. Inf. Theory*, vol. 52, no. 4, pp. 1289–1306, Apr. 2006.

[16] S. Zhang, Y. Zhu, and G. Kuang, "Imaging of downward-looking linear array three-dimensional SAR based on FFT-MUSIC," *IEEE Geosci. Remote Sens. Lett.*, vol. 12, no. 4, pp. 885–889, Apr. 2015.

[17] W. Tan, P. Huang, K. Han, Q. Liu, and X. Peng, "Array error calibration methods in downward-looking linear-array three-dimensional synthetic aperture radar," *J. Appl. Remote Sens.*, vol. 10, no. 2, 2016, Art. no. 025010.

[18] S. Jun, Z. Xiaoling, X. Gao, and J. Jianyu, "Signal processing for microwave array imaging: TDC and sparse recovery," *IEEE Trans. Geosci. Remote Sens.*, vol. 50, no. 11, pp. 4584–4598, Nov. 2012.

[19] E. J. Candes and M. B. Wakin, "An introduction to compressive sampling," *IEEE Signal Process. Mag.*, vol. 25, no. 2, pp. 21–30, Mar. 2008.

[20] X. Ren, L. Chen, and J. Yang, "3-D imaging algorithm for down-looking MIMO array SAR based on Bayesian compressive sensing," *Int. J. Antennas Propag.*, vol. 2014, 2014, Art. no. 612326.

[21] S. Zhang, Y. Zhu, G. Dong, and G. Kuang, "Truncated SVD-based compressive sensing for downward-looking three-dimensional SAR imaging with uniform/nouniform linear array," *IEEE Geosci. Remote Sens. Lett.*, vol. 12, no. 9, pp. 1853–1857, Sep. 2015.

[22] X. Peng, W. Tan, W. Hong, C. Jiang, Q. Bao, and Y. Wang, "Airborne DLSLA 3-D SAR image reconstruction by combination of polar formatting and L₁ regularization," *IEEE Trans. Geosci. Remote Sens.*, vol. 54, no. 1, pp. 213–226, Jan. 2016.

[23] Y. Chi, A. Pezeshki, L. L. Scharf, and A. R. Calderbank, "Sensitivity to basis mismatch in compressed sensing," *IEEE Trans. Signal Process.*, vol. 59, no. 5, pp. 2182–2195, May 2011.

[24] M. A. Herman and T. Strohmer, "General deviants: An analysis of perturbations in compressed sensing," *IEEE J. Sel. Topics Signal Process.*, vol. 4, no. 2, pp. 342–349, Apr. 2010.

[25] E. J. Candes, J. Romberg, and T. Tao, "Robust uncertainty principles: Exact signal reconstruction from highly incomplete frequency information," *IEEE Trans. Inf. Theory*, vol. 52, no. 2, pp. 489–509, Feb. 2006.

[26] Q. Bao, K. Han, Y. Lin, B. Zhang, J. Liu, and W. Hong, "Imaging method for downward-looking sparse linear array three-dimensional synthetic aperture radar based on reweighted atomic norm," *J. Appl. Remote Sens.*, vol. 10, no. 1, 2016, Art. no. 015008.

[27] Q. Bao, K. Han, X. Peng, W. Hong, B. Zhang, and W. Tan, "DLSLA 3-D SAR imaging algorithm for off-grid targets based on pseudo-polar formatting and atomic norm minimization," *Sci. China Inf. Sci.*, vol. 59, no. 6, 2016, Art. no. 062310.

[28] Q. Bao, X. Peng, Z. Wang, Y. Lin, and W. Hong, "DLSLA 3-D SAR imaging based on reweighted gridless sparse recovery method," *IEEE Geosci. Remote Sens. Lett.*, vol. 13, no. 6, pp. 841–845, Jun. 2016.

[29] Z. Yang, L. Xie, and C. Zhang, "Off-grid direction of arrival estimation using sparse Bayesian inference," *IEEE Trans. Signal Process.*, vol. 61, no. 1, pp. 38–43, Jan. 2013.

[30] Q. Bao, C. Jiang, Y. Lin, W. Tan, Z. Wang, and W. Hong, "Measurement matrix optimization and mismatch problem compensation for DLSLA 3-D SAR cross-track reconstruction," *Sensors*, vol. 16, no. 8, pp. 1333–1349, 2016.

[31] S.-J. Wei, X.-L. Zhang, and J. Shi, "'One-active' linear array SAR 3-D high resolution imaging via compressed sensing," in *Proc. 3rd Int. Asia-Pac. Conf. Synthetic Aperture Radar*, Seoul, South Korea, 2011, pp. 1–4.

[32] S.-J. Wei, X.-L. Zhang, and J. Shi, "Linear array SAR imaging via compressed sensing," *Prog. Electromagn. Res.*, vol. 117, pp. 299–319, 2011.

[33] S.-J. Wei, X.-L. Zhang, J. Shi, and K.-F. Liao, "Sparse array microwave 3-D imaging: Compressed sensing recovery and experimental study," *Prog. Electromagn. Res.*, vol. 135, pp. 161–181, 2013.

[34] A. Ghaffari, M. Babaie-Zadeh, and C. Jutten, "Sparse decomposition of two dimensional signals," in *Proc. IEEE Int. Conf. Acoust., Speech Signal Process.*, Apr. 2009, pp. 3157–3160.

Le Kang was born in Shaanxi, China, in 1993. He received the B.S. degree from Tsinghua University, Beijing, China, in 2015, and the M.S. degree in electrical engineering in 2017 from the Institute of Information and Navigation, Air Force Engineering University, Xi'an, China, where he is currently working toward the Ph.D. degree.

His research interests include signal processing and autotarget recognition in SAR and ISAR.

Tian-chi Sun received the M.S. degree in electrical engineering in 2017 from the Institute of Information and Navigation, Air Force Engineering University, Xi'an, China, where he is currently working toward the Ph.D. degree.

His research interests include intelligent signal processing and its application in SAR imaging.

Ying Luo (Member, IEEE) was born in Hunan, China, in 1984. He received the M.S. and Ph.D. degrees in electrical engineering from the Institute of Telecommunication Engineering, Air Force Engineering University (AFEU), Xi'an, China, in 2008 and 2013, respectively.

He was a Postdoctoral Fellow with the National Laboratory of Radar Signal Processing, Xidian University, from 2014 to 2017, and a Visiting Scholar with the Department of Electrical and Computer Engineering, National University of Singapore, Singapore, from 2017 to 2018. He is currently an Associate Professor/Ph.D. Advisor with the Institute of Information and Navigation, AFEU, Xi'an, and an Adjunct Associate Professor with the Key Laboratory for Information Science of Electromagnetic Waves, Ministry of Education, Fudan University, Shanghai, China. He has authored or coauthored three books and more than 100 papers on journals and conferences. His research interests include signal processing and autotarget recognition in SAR and ISAR.

Dr. Luo was a recipient of the First-Grade Prize of Shaanxi Natural Science Excellent Academic Paper in 2010 and 2013, respectively, for two of his papers.

Qun Zhang (Senior Member, IEEE) received the M.S. degree in mathematics from Shaanxi Normal University, Xi'an, China, in 1988, and the Ph.D. degree in electrical engineering from Xidian University, Xi'an, in 2001.

He was a Research Engineer from 2001 to 2003 and a Research Fellow from 2005 to 2006 with the Department of Electrical and Computer Engineering, National University of Singapore, Singapore. He is currently a Professor with the Institute of Information and Navigation, Air Force Engineering University, Xi'an, China, and an Adjunct Professor with the Key Laboratory for Information Science of Electromagnetic Waves, Ministry of Education, Fudan University, Shanghai, China. He has authored or coauthored more than 200 papers on journals and conferences. His main research interests include signal processing, clutter suppression, and its application in SAR and ISAR.

Jia-cheng Ni was born in Shaanxi, China, in 1990. He received the M.S. and Ph.D. degrees in electrical engineering from Air Force Engineering University (AFEU), Xi'an, China, in 2014 and 2018, respectively.

He is currently with the Radar and Signal Processing Laboratory, Institute of Information and Navigation, AFEU. His current research interests include sparse signal processing and SAR imaging.